Impurity band magnetism in organic semiconductors

Andrea Droghetti[*]

Nano-Bio Spectroscopy Group and European Theoretical Spectroscopy Facility, Materials Physics Center,
University of the Basque Country, Av.Tolosa 72, 20018 San Sebastian, Spain

Stefano Sanvito

School of Physics and CRANN Institute, Trinity College, Dublin 2, Ireland

Recent experiments and theoretical studies have proposed that spin-transport in organic semiconductors, in particular in Alq_3, may occur in an impurity band. Here we model the electronic and magnetic properties of such an impurity band by treating the effect of disorder in a numerically accurate way. The calculations are carried out by solving the Anderson-Hubbard model within the mean-field approximation and by accounting for magnetic excitations via the Bethe-Salpeter equation. We find that some impurities form clusters where electrons are delocalized, while others develop localized magnetic moments, which are antiferromagnetically correlated. The excitations of these correlated magnetic moments are spin waves, which can enable spin transport.

I. INTRODUCTION

Organic semiconductors (OSCs) made their first appearance in spintronics more than a decade ago [1–3]. Since then, many experimental studies succeeded in measuring magnetoresistance (MR) across hybrid spin-valve devices [4–9], where an OSC film is sandwiched between two ferromagnetic electrodes. Despite these important results, research in organic spintronics has been stumbling during the last few years. This is because our understanding of spin injection and transport in OSCs is still incomplete.

Over the years, intense efforts have been devoted to prove spin-injection from ferromagnetic electrodes into an OSC and to investigate the key role played by the interfaces [11–22]. Some experiments have indicated that the injection of spin-polarized charge carriers into molecular orbitals can be achieved both electrically [9,10] and optically [11]. Despite that, reports about MR in hybrid organic spin valves are often difficult to interpret even for the prototypical devices comprising Alq_3 molecules, which have been extensively studied for years. These devices are surprisingly conductive and the highest MR is measured at bias voltages of the order of 100 meV [2,4,23,24]. This contrasts with the fact that the typical electron (hole) injection barrier into the lowest unoccupied (highest occupied) molecular orbital of Alq_3 is of the order of 1 eV [9,21,25]. Furthermore, OSCs seem not to be affected by the conductivity mismatch, in contrast to their inorganic counterparts [26].

To rationalize this body of experimental findings, Yu proposed that transport through hybrid organic spin valves may occur along a broad impurity band located inside the molecule transport gap [27,28]. Such model can qualitatively explain

the typical *I-V* characteristic curve, the dependence of the MR on the bias voltage, and the absence of the conductivity mismatch problem [27]. Furthermore, it also accounts for other common phenomenological features such as the suppression of the Hanle effect [28]. Although the experimental validation of the model has still to be established, a detailed analysis of the performances of Alq_3-based spin valves does indeed strongly support the idea that transport at low bias voltages proceeds by hopping between trap states, which form an impurity band at sufficiently high concentration [29]. These impurities have been proposed to be oxygen ions O_2^- [30,31]. For devices with molecules other than Alq_3, experiments are more scarce and the possibility of impurity band transport has not been systematically analyzed to date.

The presence of the impurity band in Alq_3-based devices indicates that many charge carriers already exist at zero temperature before the application of a bias voltage. The model by Yu assumes that each impurity hosts one localized electron and therefore a magnetic moment, which is coupled to those of the neighbor impurities via direct exchange. However, this picture may not describe the most general case. Electrons may not be fully localized and magnetic moments are not guaranteed to form. This will depend on a subtle balance between the disordered impurity distribution, the overlap of their electronic wave functions, the electron-electron interaction, and the wave-function renormalization effects caused by the interaction of electrons with the molecular vibrations.

In this paper, we investigate the equilibrium electronic and magnetic properties of an impurity band. We account for the effect of disorder in an accurate way via numerical calculations and we release the assumption that each impurity hosts a localized magnetic moment. We employ a variant of the Hubbard model, namely the Anderson-Hubbard model (AHM) [32,33], where the on-site energies are allowed to assume random values. We do not aim at accessing the exact

---

*andrea.droghetti@ehu.eus

mathematical properties of the model; rather, we focus on some qualitative results that may be relevant for impurity bands in OSCs, in particular Alq$_3$. For this purpose, we treat the electron-electron interaction at the mean-field (MF) level, which already leads to quite interesting physics.

We find that the interplay between disorder and electron-electron interaction separates the impurity lattices into different regions. Some regions are almost insulating and each impurity carries a localized magnetic moment. In contrast, other regions are more metalliclike, where electrons delocalize over several impurities and no magnetic moment is formed. This behavior is reminiscent of the "two-fluid" model [34,35] introduced many years ago to explain the properties of P- and B-doped Si at low temperatures [36–38]. While, for those systems, the two-fluid model was found not to provide a satisfactory description of the experimental results, here we suggest that it should be reconsidered in the context of impurity bands in Alq$_3$ and, more in general, in OSCs. Notably, in the limit in which the itinerant component of the two fluids becomes negligible, the model reduces to that of a disordered quantum antiferromagnet [39], which shares some similarities with the model proposed by Yu for large impurity concentrations [28].

Although experiments have traditionally focused on electrical spin-injection into OSCs [40], a few studies recently reported spin injection induced via spin pumping [41–43]. While in the case of electrical spin-injection the spin is transported via diffusion of spin-polarized charge carries, in spin-pumping experiments spin waves carry the angular momentum [44]. Therefore, here we extend our investigation to examine whether spin waves can develop into an impurity band. Our results, obtained by solving the Bethe-Salpeter equation (BSE) [45], show that indeed spin waves can appear in the regions of an impurity lattice where the localized magnetic moments are present. Accordingly, we propose that, while charge currents propagate through the metallic component of the two fluids, spin currents are transported through the insulating one.

The paper is organized as follows. In Sec. II, we first introduce the AHM (Sec. II A) and the theoretical methods (Secs. II B and II C). Then we discuss in detail the MF results in Sec. III and the calculations of the spin waves in Sec. IV. Finally, in Sec. V we summarize the main outcomes of our paper and we relate them to the physics of the impurity band in OSCs.

II. MODEL AND METHODS

A. Anderson-Hubbard model

Impurities in an OSC film form an impurity band with a broad energy distribution located inside the molecule transport gap. In particular, recent experiments have focused on Alq$_3$ molecules proposing oxygen ions as the relevant impurities [30]. Such impurity band is described here by means of the so-called AHM, which is defined by the Hamiltonian

$$\hat{\mathcal{H}} = \sum_{\mathbf{i},\sigma=\uparrow,\downarrow} \epsilon_{\mathbf{i}} \hat{n}_{\mathbf{i}\sigma} - t \sum_{\mathbf{i},\sigma=\uparrow,\downarrow} \left(\hat{c}^\dagger_{\mathbf{i}+1\sigma} \hat{c}_{\mathbf{i}\sigma} + H.c. \right)$$
$$+ U \sum_{\mathbf{i}} \hat{n}_{\mathbf{i}\uparrow} \hat{n}_{\mathbf{i}\downarrow}. \quad (1)$$

Here, $\hat{n}_{\mathbf{i}\sigma} = \hat{c}^\dagger_{\mathbf{i}\sigma} \hat{c}_{\mathbf{i}\sigma}$ is the spin-dependent occupation number operator of site $\mathbf{i}$, $t > 0$ is the hopping probability amplitude between two nearest-neighbors sites, $U \geqslant 0$ is the screened Coulomb interaction strength and $\epsilon_{\mathbf{i}}$ represents the on-site energy for site $\mathbf{i}$. This is assumed to be a random variable drawn from a Gaussian distribution with variance Δ^2. The random on-site energies describe the fluctuation of the electrostatic environment around an impurity. In principle, the hopping probability can also be chosen as a random variable. However, for atoms or small dopant molecules embedded in organic solid-state materials, the on-site Coulomb interaction and electrostatic effects are quite large [46], while the hopping is generally very small, i.e., $\Delta \gg t$ and $U \gg t$ (see also the discussion in Sec. V). Therefore, we have decided not to include random hoppings to reduce the complexity of the model. Furthermore, we note that a few test calculations we performed indicate that the qualitative picture presented in the following would not change if random hopping probabilities were considered. Finally, we work at zero temperature and we neglect the electron-vibration interaction, although this often plays an important role in the behavior of organic materials [47,48]. The extension of the model to include the electron-vibration interaction and finite temperature effects is left for future studies.

All results presented here are for a three-dimensional (3D) cubic lattice of linear dimension L, i.e., the total number of sites is $N = L^3$.

B. The mean-field approximation

The MF Hamiltonian for the AHM reads

$$\hat{\mathcal{H}}_{\mathrm{MF}} = \sum_{\mathbf{i},\sigma=\uparrow,\downarrow} (\epsilon_{\mathbf{i}} + U \langle \hat{n}_{\mathbf{i}-\sigma} \rangle) \hat{c}^\dagger_{\mathbf{i}\sigma} \hat{c}_{\mathbf{i}\sigma} - t \sum_{\mathbf{i},\sigma=\uparrow,\downarrow} \hat{c}^\dagger_{\mathbf{i}+1\sigma} \hat{c}_{\mathbf{i}\sigma}. \quad (2)$$

The eigenenergies and eigenstates are $\epsilon_{\alpha\sigma}$ and $|\alpha\sigma\rangle = \hat{c}^\dagger_{\alpha\sigma} |-\rangle$ ($|-\rangle$ is the vacuum), i.e.,

$$\hat{\mathcal{H}}_{\mathrm{MF}} |\alpha\sigma\rangle = \epsilon_{\alpha\sigma} |\alpha\sigma\rangle. \quad (3)$$

The expectation value $\langle \hat{n}_{\mathbf{i}\sigma} \rangle = \langle 0_{\mathrm{MF}} | \hat{n}_{\mathbf{i}\sigma} | 0_{\mathrm{MF}} \rangle$ is taken over the MF ground state,

$$|0_{\mathrm{MF}}\rangle = \prod_{\epsilon_{\alpha\uparrow} \leqslant E_F} \hat{c}^\dagger_{\alpha\uparrow} \prod_{\epsilon_{\beta\downarrow} \leqslant E_F} \hat{c}^\dagger_{\beta\downarrow} |-\rangle, \quad (4)$$

where E_F is the Fermi energy. The operators $\hat{c}_{\mathbf{i}\sigma}$ ($\hat{c}^\dagger_{\mathbf{i}\sigma}$) and $\hat{c}_{\alpha\sigma}$ ($\hat{c}^\dagger_{\alpha\sigma}$) are connected by the unitary transformations:

$$\hat{c}^\dagger_{\alpha\sigma} = \sum_{\mathbf{i}} u_{\alpha\mathbf{i}\sigma} \hat{c}^\dagger_{\mathbf{i}\sigma}, \quad (5)$$

$$\hat{c}_{\alpha\sigma} = \sum_{\mathbf{i}} u^*_{\alpha\mathbf{i}\sigma} \hat{c}_{\mathbf{i}\sigma}. \quad (6)$$

Then, the local spin-dependent occupation of site $\mathbf{i}$ is given by

$$\langle \hat{n}_{\mathbf{i}\sigma} \rangle = \sum_{\alpha\sigma}^{E_F} u^*_{\alpha\mathbf{i}\sigma} u_{\alpha\mathbf{i}\sigma}, \quad (7)$$

where the sum runs over all states with $\epsilon_{\alpha\sigma} \leqslant E_F$.

Since the MF Hamiltonian of Eq. (2) depends on $\langle \hat{n}_{\mathbf{i}\sigma} \rangle$, which, in turn, is calculated by using the the eigenvectors defined in Eq. (6), an iterative self-consistent solution is required.

The MF total energy is

$$E_{\mathrm{MF}} = \sum_{\alpha\uparrow,\beta\downarrow}^{E_F} (\epsilon_{\alpha\uparrow} + \epsilon_{\beta\downarrow}) - U \sum_{\alpha\uparrow,\beta\downarrow}^{E_F} \sum_{\mathbf{i}} u^*_{\alpha\mathbf{i}\uparrow} u_{\alpha\mathbf{i}\uparrow} u^*_{\beta\mathbf{i}\downarrow} u_{\beta\mathbf{i}\downarrow}, \quad (8)$$

where the sums run over the states with $\epsilon_{\alpha\uparrow} \leqslant E_F$ and $\epsilon_{\beta\downarrow} \leqslant E_F$.

The magnetic excitations are readily calculated in the MF framework. These have a single-particle character (Stoner excitations) and energies $\omega_n^{\mathrm{MF}} = (\epsilon_{p\sigma} - \epsilon_{h-\sigma})$, where the index $p\sigma$ ($h\sigma$) labels a generic unoccupied (occupied) MF state (i.e., $\alpha\sigma \equiv p\sigma$ if $\epsilon_{\alpha\sigma} > E_F$ and $\alpha\sigma \equiv h\sigma$ if $\epsilon_{\alpha\sigma} \leqslant E_F$). Unfortunately, the MF approximation does not account for the low-lying collective magnetic excitations (spin waves). These can be calculated by employing the many-body perturbation theory.

C. The Bethe-Salpeter equation

The time-dependent spin-spin correlation function is

$$C_{\mathbf{ij}}(t, 0) = -i\langle 0|T\{\hat{S}^-_{\mathbf{i}}(t)\hat{S}^+_{\mathbf{j}}(0)\}|0\rangle, \quad (9)$$

where $\hat{S}^-_{\mathbf{i}}(t)$ [$\hat{S}^+_{\mathbf{j}}(0)$] denotes the operator $\hat{S}^-_{\mathbf{i}} = \hat{c}^\dagger_{\mathbf{i}\downarrow}\hat{c}_{\mathbf{i}\uparrow}$ ($\hat{S}^+_{\mathbf{i}} = \hat{c}^\dagger_{\mathbf{i}\uparrow}\hat{c}_{\mathbf{i}\downarrow}$) in the Heisenberg picture. The state $|0\rangle$ represents the true many-particle ground state of the AHM to be distinguished from the MF ground state, $|0_{\mathrm{MF}}\rangle$, defined in Eq. (4). $T\{...\}$ denotes the time-ordered product. The time-Fourier transform of $C_{\mathbf{ij}}(t, 0)$ defines the dynamic transverse spin susceptibility [49],

$$\chi^{-+}_{\mathbf{ij}}(\omega) = \int_{-\infty}^{\infty} dt\, e^{i\omega t} C_{\mathbf{ij}}(t, 0), \quad (10)$$

which can be expressed in the Lehmann representation [45]:

$$\chi^{-+}_{\mathbf{ij}}(\omega) = \sum_n \left[\frac{\langle 0|\hat{S}^-_{\mathbf{i}}|n\rangle \langle n|\hat{S}^+_{\mathbf{j}}|0\rangle}{\omega - \omega_n + i\eta} - \frac{\langle 0|\hat{S}^+_{\mathbf{j}}|n\rangle \langle n|\hat{S}^-_{\mathbf{i}}|0\rangle}{\omega + \omega_n - i\eta} \right]. \quad (11)$$

In Eq. (11), the limit $\eta \to 0^+$ is implied and $|n\rangle$ is an nth many-particle excited state of energy E_n, $\omega_n = E_n - E_0$, with E_0 the ground-state energy. The Lehmann representation explicitly shows that the poles of $\chi^{-+}_{\mathbf{ij}}(\omega)$ represent the energies of the collective magnetic excitations, i.e., the spin waves.

The dynamic transverse spin susceptibility of Eq. (10) is calculated by using the BSE. In the ladder diagram approximation, it is written as [50]

$$\chi^{-+}_{\mathbf{ij}}(\omega) = {}^0\chi^{-+}_{\mathbf{ij}}(\omega) - U \sum_{\mathbf{k}} {}^0\chi^{-+}_{\mathbf{ik}}(\omega)\chi^{-+}_{\mathbf{kj}}(\omega), \quad (12)$$

where ${}^0\chi^{-+}_{\mathbf{ij}}(\omega)$ is the MF transverse spin susceptibility. This

is defined as

$${}^0\chi^{-+}_{\mathbf{ij}}(\omega) = \int_{-\infty}^{\infty} dt\, e^{i\omega t} C^{\mathrm{MF}}_{\mathbf{ij}}(t, 0), \quad (13)$$

with $C^{\mathrm{MF}}_{\mathbf{ij}}(t, 0) = -i\langle 0_{\mathrm{MF}}|T\{\hat{S}^-_{\mathbf{i}}(t)\hat{S}^+_{\mathbf{j}}(0)\}|0_{\mathrm{MF}}\rangle$. Its Lehmann representation reads

$${}^0\chi^{-+}_{\mathbf{ij}}(\omega)$$
$$= \sum_{p\uparrow,h\downarrow} \frac{u^*_{p\mathbf{i}\uparrow} u_{h\mathbf{i}\downarrow} u^*_{h\mathbf{j}\downarrow} u_{p\mathbf{j}\uparrow}}{\omega - \epsilon_{p\uparrow} + \epsilon_{h\downarrow} + i\eta} - \sum_{h\uparrow,p\downarrow} \frac{u^*_{h\mathbf{i}\uparrow} u_{p\mathbf{i}\downarrow} u^*_{p\mathbf{j}\downarrow} u_{h\mathbf{j}\uparrow}}{\omega + \epsilon_{p\downarrow} - \epsilon_{h\uparrow} - i\eta}, \quad (14)$$

where again the limit $\eta \to 0^+$ is implied. The poles of ${}^0\chi^{-+}_{\mathbf{ij}}(\omega)$ are the Stoner excitations (see the discussion at the end of Sec. II B).

As pointed out by Szczech *et al.* [51], the determination of the collective magnetic excitations turns out to be a particularly simple problem in the case of the AHM. In fact, the symmetric matrix ${}^0\chi^{-+}(\omega)$, whose elements are ${}^0\chi^{-+}_{\mathbf{ij}}(\omega)$, can be diagonalized by an orthogonal matrix $V(\omega)$ giving the eigenvalues $\{\lambda_\gamma(\omega)\}$ (if ω does not coincide with the energy of a Stoner excitation). Notably, $V(\omega)$ also diagonalizes the matrix $\chi^{-+}(\omega)$ of elements $\chi^{-+}_{\mathbf{ij}}(\omega)$. Thus, by solving the BSE, we obtain

$$\sum_{\mathbf{ij}} V_{\gamma\mathbf{i}} \chi^{-+}_{\mathbf{ij}}(\omega) V_{\mathbf{j}\gamma} = \frac{\lambda_\gamma(\omega)}{1 + U\lambda_\gamma(\omega)}. \quad (15)$$

As the poles of $\chi^{-+}_{\mathbf{ij}}(\omega)$ coincide with the collective magnetic excitations, these are given by the relation

$$1 + U\lambda_\gamma(\omega) = 0. \quad (16)$$

In other words, the value of ω (not equal to the Stoner excitation energies), for which one of the eigenvalues of ${}^0\chi^{-+}$ satisfies Eq. (16), represents the energy of a collective magnetic excitation.

Interestingly, an alternative approach to calculate the collective magnetic excitations consists of reformulating the BSE as a generalized eigenvalue problem [45]. This is equivalent to introduce an effective Hamiltonian acting on a selected range of particle-hole states of opposite spin. The collective magnetic excitations are then described as a linear combination of processes which transfer a particle from one occupied state to an unoccupied state of opposite spin.

To begin, the BSE is rewritten over the basis that diagonalizes the MF Hamiltonian. By using the unitary transformations of Eqs. (5) and (6), we obtain

$$\chi^{-+}_{\beta\alpha\gamma\delta}(\omega) = {}^0\chi^{-+}_{\beta\alpha\gamma\delta}(\omega)$$
$$+ - U \sum_{\mathbf{i}} \sum_{\epsilon,\zeta,\eta,\theta} u_{\epsilon\mathbf{i}\uparrow} u^*_{\zeta\mathbf{i}\downarrow} u_{\eta\mathbf{i}\downarrow} u^*_{\theta\mathbf{i}\uparrow}$$
$$\times {}^0\chi^{-+}_{\beta\alpha\epsilon\zeta}(\omega) \chi^{-+}_{\theta\eta\gamma\delta}(\omega), \quad (17)$$

where $\chi^{-+}_{\beta\alpha\gamma\delta}(\omega)$ is a short-hand notation for $\chi^{-+}_{\beta\uparrow,\alpha\downarrow,\gamma\uparrow,\delta\downarrow}(\omega)$. This indicates the Fourier transform of

$$C_{\beta\uparrow,\alpha\downarrow,\gamma\uparrow,\delta\downarrow}(t,0) = -i\langle 0|T\{\hat{c}^\dagger_{\alpha\downarrow}(t)\hat{c}_{\beta\uparrow}(t)\hat{c}^\dagger_{\gamma\uparrow}(0)\hat{c}_{\delta\downarrow}(0)\}|0\rangle.$$

Then we can distinguish two possible cases

$$\chi^{-+}_{ph\gamma\delta}(\omega) = \frac{1}{\omega - \epsilon_{p\uparrow} + \epsilon_{h\downarrow} + i\eta}\left\{\delta_{h\downarrow,\delta\downarrow}\delta_{p\uparrow,\gamma\uparrow}\right.$$
$$-U\sum_{\mathbf{i}}\sum_{h'\downarrow,p'\uparrow} u_{p\mathbf{i}\uparrow}u^*_{h\mathbf{i}\downarrow}u_{h'\mathbf{i}\downarrow}u^*_{p'\mathbf{i}\uparrow}\chi^{-+}_{p'h'\gamma\delta}(\omega)$$
$$\left. -U\sum_{\mathbf{i}}\sum_{p'\downarrow,h'\uparrow} u_{p\mathbf{i}\uparrow}u^*_{h\mathbf{i}\downarrow}u_{p'\mathbf{i}\downarrow}u^*_{h'\mathbf{i}\uparrow}\chi^{-+}_{h'p'\gamma\delta}(\omega)\right\},$$

(18)

$$\chi^{-+}_{hp\gamma\delta}(\omega) = -\frac{1}{\omega + \epsilon_{p\downarrow} - \epsilon_{h\uparrow} - i\eta}\left\{\delta_{p\downarrow,\delta\downarrow}\delta_{h\uparrow,\gamma\uparrow}\right.$$
$$-U\sum_{\mathbf{i}}\sum_{p'\downarrow,h'\uparrow} u_{h\mathbf{i}\uparrow}u^*_{p\mathbf{i}\downarrow}u_{p'\mathbf{i}\downarrow}u^*_{h'\mathbf{i}\uparrow}\chi^{-+}_{h'p'\gamma\delta}(\omega)$$
$$\left. -U\sum_{\mathbf{i}}\sum_{h'\downarrow,p'\uparrow} u_{h\mathbf{i}\uparrow}u^*_{p\mathbf{i}\downarrow}u_{h'\mathbf{i}\downarrow}u^*_{p'\mathbf{i}\uparrow}\chi^{-+}_{p'h'\gamma\delta}(\omega)\right\}.$$

(19)

Here we have used the fact that ${}^0\chi^{-+}_{hp\epsilon\zeta}(\omega)$ is not zero only for $\epsilon = h$ and $\zeta = p$, and similarly ${}^0\chi^{-+}_{phe\zeta}(\omega)$ is not zero only for $\epsilon = p$ and $\zeta = h$. Furthermore, ${}^0\chi^{-+}_{hphp}(\omega)$ and ${}^0\chi^{-+}_{phph}(\omega)$ have been expressed through their Lehmann representation [see Eq. (14)].

Equations (18) and (19) can then be written in matrix form:

$$\begin{pmatrix} -\omega + \mathbf{A} & \mathbf{B} \\ \mathbf{B}^* & \omega + \mathbf{C} \end{pmatrix}\begin{pmatrix} \chi^{-+}_{ph\gamma\delta}(\omega) \\ \chi^{-+}_{hp\gamma\delta}(\omega) \end{pmatrix} = \begin{pmatrix} -\delta_{p\uparrow,\gamma\uparrow}\delta_{h\downarrow,\delta\uparrow} \\ -\delta_{h\uparrow\gamma\uparrow}\delta_{p\downarrow,\delta\downarrow} \end{pmatrix}.$$

(20)

The matrices **A**, **B**, and **C** have components

$$A_{p\uparrow h\downarrow,p'\uparrow h'\downarrow} = (\epsilon_{p\uparrow} - \epsilon_{h\downarrow})\delta_{p\uparrow h\downarrow,p'\uparrow h'\downarrow}$$
$$-U\sum_{\mathbf{i}} u_{p\mathbf{i}\uparrow}u^*_{h\mathbf{i}\downarrow}u^*_{p'\mathbf{i}\uparrow}u_{h'\mathbf{i}\downarrow}$$

(21)

$$B_{p\uparrow h\downarrow,p'\downarrow h'\uparrow} = -U\sum_{\mathbf{i}} u_{p\mathbf{i}\uparrow}u^*_{h\mathbf{i}\downarrow}u_{p'\mathbf{i}\downarrow}u^*_{h'\mathbf{i}\uparrow},$$

(22)

$$C_{p\downarrow h\uparrow,p'\downarrow h'\uparrow} = (\epsilon_{p\downarrow} - \epsilon_{h\uparrow})\delta_{p\downarrow h\uparrow,p'\downarrow h'\uparrow}$$
$$-U\sum_{\mathbf{i}} u^*_{p\mathbf{i}\downarrow}u_{h\mathbf{i}\uparrow}u_{p'\mathbf{i}\downarrow}u^*_{h'\mathbf{i}\uparrow}.$$

(23)

As shown by Eq. (20), the transverse magnetic susceptibility diverges when

$$\det\begin{pmatrix} -\omega + \mathbf{A} & \mathbf{B} \\ \mathbf{B}^* & \omega + \mathbf{C} \end{pmatrix} = 0.$$

(24)

Therefore, the magnetic excitations are calculated by solving the matrix eigenvalue equation:

$$\begin{pmatrix} \mathbf{A} & \mathbf{B} \\ -\mathbf{B}^* & -\mathbf{C} \end{pmatrix}\begin{pmatrix} \mathbf{X}^n \\ \mathbf{Y}^n \end{pmatrix} = \omega_n\begin{pmatrix} \mathbf{X}^n \\ \mathbf{Y}^n \end{pmatrix}.$$

(25)

The matrix on the left-hand side is called RPA matrix and it has dimension $[(N_{h\uparrow}N_{p\downarrow}) + (N_{h\downarrow}N_{p\uparrow})] \times [(N_{h\uparrow}N_{p\downarrow}) + (N_{h\downarrow}N_{p\uparrow})]$, where $N_{h\sigma}$ ($N_{p\sigma}$) is the number of occupied (unoccupied) states of spin σ.

Although the RPA matrix is manifestly not hermitian, the eigenvalues ω_n will be real if the MF ground state is a stable one. A complex value for ω_n signals that $|0_{\rm MF}\rangle$ is unstable [52].

Real eigenvalues can be either positive or negative, with positive (negative) eigenvalues corresponding to the positive (negative) poles of $\chi^{-+}_{ij}(\omega)$. In addition, it is easy to demonstrate that $\chi^{+-}_{ij}(\omega) = \chi^{-+}_{ji}(-\omega)$ with $\chi^{+-}_{ij}(\omega) = -i\int_{-\infty}^\infty dt\langle 0|T\{\hat{S}^+_i(t)\hat{S}^-_j(0)\}|0\rangle$. Finally, when the MF solution breaks the spin-rotational symmetry, eigenvalues equal to zero also occur (Goldstone modes) [53,54].

$\mathbf{X}^n$ and $\mathbf{Y}^n$ are column vectors of elements $X^n_{p\uparrow h\downarrow}$ and $Y^n_{h\uparrow p\downarrow}$: These represent the coefficients of the expansion of an excited state $|n_{\rm RPA}\rangle$ with energy ω_n (for $\omega_n > 0$) over the electron-hole pairs of opposite spin; namely,

$$|n_{\rm RPA}\rangle = \hat{Q}^\dagger_n|0_{\rm RPA}\rangle,$$
$$\hat{Q}^\dagger_n = \sum_{p\uparrow,h\downarrow} X^n_{p\uparrow h\downarrow}\hat{c}^\dagger_{p\uparrow}\hat{c}_{h\downarrow} - \sum_{p\downarrow,h\uparrow} Y^n_{h\uparrow p\downarrow}\hat{c}^\dagger_{h\uparrow}\hat{c}_{p\downarrow}, \quad (26)$$

with $|0_{\rm RPA}\rangle$ being the RPA ground state defined by $Q_n|0_{\rm RPA}\rangle = 0$. Similarly, the eigenstates that correspond to $\omega_n < 0$ are de-excitations and read

$$|0_{\rm RPA}\rangle = \hat{Q}_n|n_{\rm RPA}\rangle,$$
$$\hat{Q}_n = \sum_{p\uparrow,h\downarrow} X^{n*}_{p\uparrow h\downarrow}\hat{c}^\dagger_{h\downarrow}\hat{c}_{p\uparrow} - \sum_{p\downarrow,h\uparrow} Y^{n*}_{h\uparrow p\downarrow}\hat{c}^\dagger_{p\downarrow}\hat{c}_{h\uparrow}. \quad (27)$$

Therefore, the RPA matrix describes an effective Hamiltonian acting over electron-hole pairs of opposite spin.

As the RPA eigenvectors are orthogonal and can be properly normalized [45,52,54], the operators $\hat{Q}_n$ and $\hat{Q}^\dagger_n$ are quasiboson operators; namely, they satisfy boson commutation relations in the weak sense,

$$\langle[\hat{Q}_m, \hat{Q}^\dagger_n]\rangle = \delta_{mn}, \quad (28)$$

$$\langle[\hat{Q}_m, \hat{Q}_m]\rangle = 0, \quad (29)$$

$$\langle[\hat{Q}^\dagger_m, \hat{Q}^\dagger_n]\rangle = 0, \quad (30)$$

where $\langle...\rangle$ indicates, as before, the average on the MF ground state.

Finally, we mention that Eq. (25) can also be obtained by the inverse procedure. This means that we can first define the operator $\hat{Q}_n$ and then calculate its equation of motion. After replacing every product of four operators $\hat{c}^\dagger\hat{c}\hat{c}^\dagger\hat{c}$ with its MF expression $\langle\hat{c}^\dagger\hat{c}\rangle\hat{c}^\dagger\hat{c}$, this procedure ultimately leads to the RPA matrix eigenvalue problem [52,54].

III. MEAN-FIELD RESULTS

In this section, we will present a detailed analysis of the MF results as a function of the screened interaction U/t and of parameter Δ/t, which we use to quantify the disorder (see Sec. II A). All results refer to cubic lattices of linear dimension $L = 8$ (i.e., $N = 8^3$), unless explicitly stated otherwise.

We note that Tusch and Logan [32] have already considered the half-filling case (i.e., when the total number of electrons is equal to the number of lattice sites N). They have showed that, while the system with no disorder is either a

Slater or a Mott insulator with a Neel-type antiferromagnetic order, disorder tends to close the gap between the lower and upper Hubbard band and a large portion of the phase diagram is then either metallic or Anderson insulating. The magnetic order is still mainly antiferromagnetic, but disorder removes the Fermi surface nesting of the simple cubic lattice in 3D. As a result, a paramagnetic phase can even appear for $U > 0$. We note that very similar results (at least at a qualitative level) were recently found also by using state-of-the-art dynamical mean-field theory calculations [55].

In our paper, we consider different numbers of electrons, besides the special case of half-filling, for which we have reproduced the results by Tusch and Logan [32]. For most of the situations inspected, we have eventually found that the overall phenomenology is similar, independent of the number of electrons. We therefore present only results for $N/2$ electrons, which corresponds to quarter filling. The system in absence of disorder is a metal and the MF approximation returns a first-order phase transition from a paramagnetic to a ferromagnetic ground state at $U/t \approx 3.5$, as observed before [56]. However, we will see that these ferromagnetic correlations are completely washed out by the disorder, while antiferromagnetic correlations between some of the sites appear.

Although the model investigated is very general and, in principle, can be (and has been) used to represent an impurity band in any semiconductor, we remark that our study aims at addressing whether some of our results can account for the general phenomenology proposed for Alq$_3$ and more generally OSCs [27–30]. This will be discussed in Sec. V.

A. General considerations about the self-consistent solution

When MF calculations are performed, different starting states generally give different final self-consistent solutions. This is because the potential energy surface can have many local minima, where the calculation may end up. The search for the true MF ground state is therefore very complicated. To explore as many states as possible we have chosen several initial conditions and compared their total energies defined in Eq. (8). These initial conditions correspond to:

(1) A ferromagnetic fully spin-polarized state with $\langle \hat{n}_{\mathbf{i}\uparrow} \rangle = 0.5$ and $\langle \hat{n}_{\mathbf{i}\downarrow} \rangle = 0.0$ for all sites

(2) A ferromagnetic slightly spin-polarized state with $\langle \hat{n}_{\mathbf{i}\uparrow} \rangle = 0.3$ and $\langle \hat{n}_{\mathbf{i}\downarrow} \rangle = 0.2$ for all sites

(3) A Neel-type antiferromagnetic state

(4) A paramagnetic state

(5) Many different magnetically disordered states obtained by randomly selecting the charge and the spin of every site with the constraint that $\sum_{\mathbf{i}} [\langle \hat{n}_{\mathbf{i}\uparrow} \rangle + \langle \hat{n}_{\mathbf{i}\downarrow} \rangle] = N/2$

In addition, we have also performed calculations starting from configurations obtained at finite temperature and then gradually reduced the temperature to approach the zero-limit. This sometimes improves the convergence to the real MF ground state, preventing the calculation from ending in metastable minima.

The local electronic and magnetic properties of the lattice in the MF ground state are studied by looking at the occupation and magnetization of each site:

$$\langle \hat{m}_{\mathbf{i}} \rangle = \langle \hat{n}_{\mathbf{i}\uparrow} \rangle - \langle \hat{n}_{\mathbf{i}\downarrow} \rangle. \quad (31)$$

These are averaged over many disorder realizations. We perform arithmetic averages. Although this may be not appropriate for disordered electronic systems in general [55], we have found that the results we obtained are adequate for the purpose of this paper.

The magnetic configuration of a state is characterized through the Fourier transform of the z component of the magnetization [32,57]:

$$S_z(\mathbf{k}) = \frac{1}{L^3} \sum_{\mathbf{i}} \langle \hat{m}_{\mathbf{i}} \rangle e^{i\mathbf{k}\mathbf{i}}. \quad (32)$$

$|S_z(\mathbf{k})|$ has a sharp peak at $\mathbf{k}a = (0, 0, 0)$ for a ferromagnetic state and at $\mathbf{k}a = (\pi, \pi, \pi)$ for an antiferromagnetic state.

Following common practice in semiconductor physics, we compute the inverse participation ratio (IPR) to analyze whether the system is insulating or metallic. The IPR [58] is defined as (see, for example, Ref. [58])

$$\text{IPR}(E_{\alpha\sigma}) = \frac{\sum_{\mathbf{i}} |u_{\mathbf{i}\alpha\sigma}|^4}{\left(\sum_{\mathbf{i}} |u_{\mathbf{i}\alpha\sigma}|^2 \right)^2}. \quad (33)$$

The IPR gives us a direct measure of the degree of localization of a state. For a state $|\alpha\sigma\rangle$ delocalized over $N_{\alpha\sigma}$ sites, we have

$$\text{IPR}(E_{\alpha\sigma}) \approx \frac{1}{N_{\alpha\sigma}}. \quad (34)$$

Therefore, the IPR is equal to zero in the thermodynamic limit for a completely delocalized state. In a finite system, the localization threshold can be derived from finite-size scaling arguments [32,59] and it is

$$\text{IPR}_c \approx 1.14/(L^3)^{0.48}. \quad (35)$$

A state, for which IPR > IPR$_c$, has to be considered localized [note that IPR$_c$ in Eq. (35) was derived at half-filling and, as discussed in the following section, one cannot ensure that it also applies for other cases]. Before going through the results in the next subsection, we point out a few general features:

(i) A paramagnetic ground state is found independently from the initial condition for small U/t (between about 1.2 and 0.2) and for any Δ/t.

(ii) When increasing the value of U/t above ~ 1.5, the calculations initiated from a paramagnetic state do not converge.

(iii) For intermediate U/t (typically $1 \lesssim U/t \lesssim 15$, but this interval generally depends on Δ/t) all the calculations, initiated at a disordered or a ferromagnetic initial state, converge to a disordered final state. However, this final state is usually not the same for different initial conditions. In the next section, we will describe better what we mean by disordered state. For the moment, it is enough to say that in such disordered state a clear magnetic order cannot be recognized, although many sites present a quite large magnetic moment. This can be better understood by looking at Fig. 1(a), which shows $|S_z(\mathbf{k})|$, in the (k_x, k_y) plane at $k_z = 0$, for a specific realization of a disordered magnetic state. We observe many peaks at different values of (k_x, k_y) but none of them dominates over the others.

(iv) For the same intermediate U/t as in (iii), an antiferromagnetic initial condition leads to a solution very similar to the disordered state, but with an enhanced peak at $\mathbf{k} = (\pi/a, \pi/a, \pi/a)$ [see, for example, Fig. 1(b)]. This seems
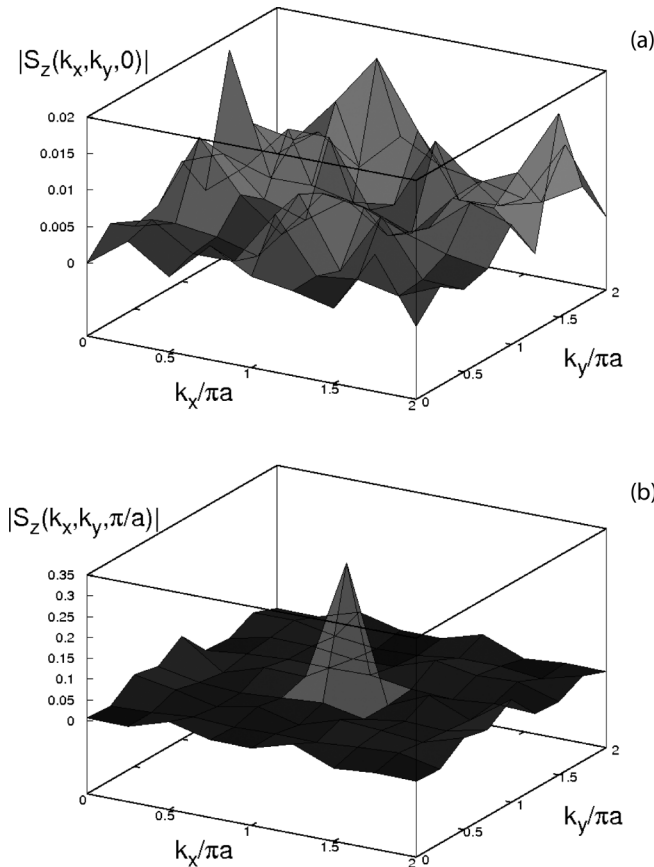
FIG. 1. Example of (a) $S_z(\mathbf{k})$ in the (k_x, k_y) plane at $k_z = 0$ for the disordered magnetic phase and (b) $S_z(\mathbf{k})$ in the (k_x, k_y) plane at $k_z = \pi/a$ for the disordered magnetic phase, with a clear highly frustrated Neel-type antiferromagnetic order. These results are obtained for a lattice with $L = 8$.

to indicate that, although the systems is still disordered, the magnetic moments of some sites tend to assume an antiferromagnetic order. An analysis of the total energies shows that solutions which capture this tendency toward antiferromagnetism always have the lowest energy for $U/t \gtrsim 6$ and $\Delta/t \gtrsim 2$.

(v) For large values of U/t, the tendency toward antiferromagnetism is further enhanced. The peak at $\mathbf{k} = (\pi/a, \pi/a, \pi/a)$ becomes sharper, while the energy difference between solutions obtained from ferromagnetic and antiferromagnetic initial conditions becomes systematically larger.

(vi) As already found by Tusch and Logan [32] for the half-filling case, only the magnetic order usually depends on the initial condition, while the total occupation $\langle \hat{n}_\mathbf{i} \rangle$ and the magnitude of the magnetic moment $|\langle \hat{m}_\mathbf{i} \rangle|$ at each site $\mathbf{i}$ do not. These quantities are indeed determined only by the values of the on-site energies.

B. Detailed description of the results

We first look at the electronic properties of the AHM and then we focus on the magnetic ones. The analysis of the average distribution of the magnetic moments inside the
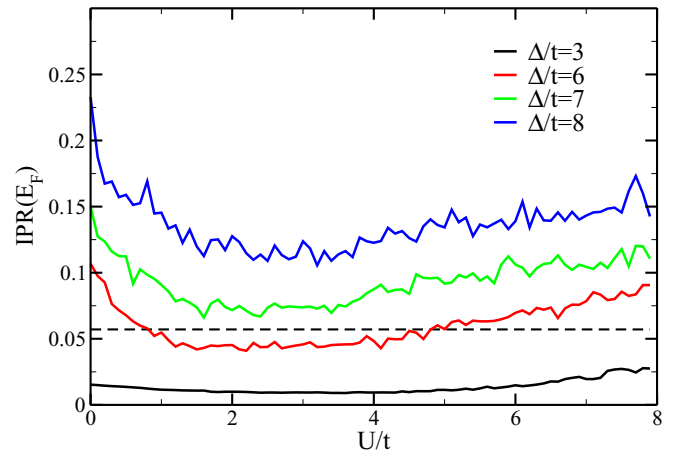

FIG. 2. IPR for the state at the Fermi energy as a function of U/t for $\Delta/t = 3$ (black line), $\Delta/t = 6$ (red line), $\Delta/t = 7$ (green line), and $\Delta/t = 8$ (blue line). The dashed horizontal line indicates the critical IPR value.

lattice will be the key part of this section within the context of impurity-band spin transport.

The electronic properties of the AHM can be analyzed by inspecting the IPR for the state closer in energy to the Fermi level. If the computed IPR is smaller than the critical IPR, calculated through Eq. (35), we will say that the system is metallic. Otherwise, we will call it an Anderson insulator. Yet, to be precise, we remark that from our data for a single system size, we cannot make any strong claim about a true metal-insulator transition as we cannot ensure that the localization threshold in Eq. (35) derived at half-filling [32,59] is also valid away from that specific case. We therefore use the IPR to infer trends toward localization/delocalization that we associate to a more metalliclike/insulatinglike character.

Figure 2 shows the IPR for the state at the Fermi level (after performing an average over hundreds of different disorder realizations) as a function of the interaction strength U/t and for several values of Δ/t. For $U/t = 0$, the system is metallic for $\Delta/t = 3$ and then becomes insulating at about $\Delta/t = 6, 7, 8$. For $2 < U/t < 5$, the interaction promotes an increase in the localization lengths of the state at the Fermi level for all Δ/t. For $\Delta/t \approx 6$, one can even observe a transition back to the metallic state at $U/t \approx 5$. This effect, observed also at half-filling, was explained as due to an interaction-induced narrowing of the effective probability distribution for the energy of each site [32].

We now turn to the magnetic properties, which are most relevant for our study. In Fig. 3, we sketch a "magnetic" phase diagram, where the phase boundary is established by looking at the parameter range where the paramagnetic MF ground state becomes unstable. This is signaled by the appearance of some complex eigenvalues for the RPA matrix (the error bar in Fig. 3 accounts for the statistical error due to the average over 100 different disorder realizations for each value of U/t and Δ/t). The phase diagram shows that the ground state is always paramagnetic for very small U/t. The charge does not spread uniformly over the lattice, but it is distributed according to the on-site energies. When U/t becomes larger, a magnetic moment forms in some of the sites and the
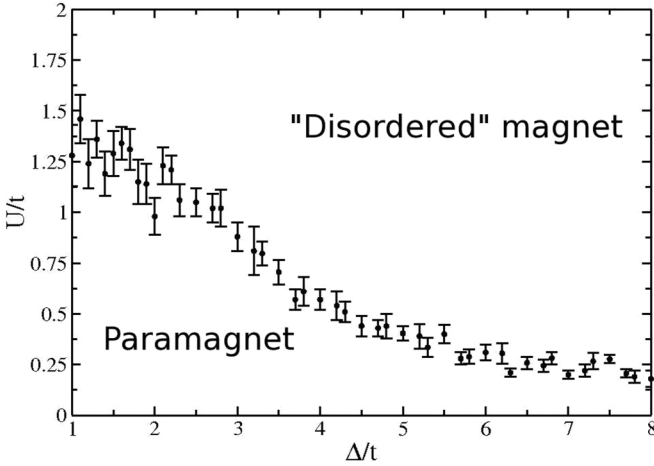
FIG. 3. Phase diagram for the MF AHM, which shows the border between the paramagnetic and the disordered magnetic phase.
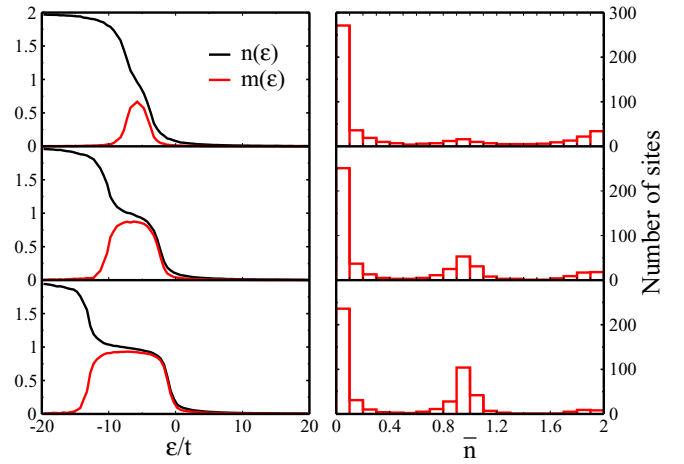

FIG. 4. Left-hand side: Mean charge and magnetization as a function of the on-site energy, i.e., $n(\epsilon)$ and $m(\epsilon)$ defined in Eq. (36). Right-hand side: Histograms displaying the average number of sites that have a given occupation $\bar{n}$ between 0 and 2 (the bin width is 0.1). The results are for $\Delta/t = 8$ and $U/t = 4$ (upper panels), $\Delta/t = 8$ and $U/t = 8$ (central panels), $\Delta/t = 8$ and $U/t = 12$ (lower panels).

disordered phase, which was mentioned in the previous subsection, appears. Notably, for increasing Δ/t, the paramagnetic phase tends to vanish and a few magnetic moments are found to form already for small U/t.

We should remark here that a disordered magnetic phase, which is intermediate between the paramagnetic and the antiferromagnetic ones, is also found in the half-filling case for lattices with $L = 8$ (and smaller) [32]. However, in that case, the disordered magnetic phase presents very small magnetic moments $|m_{\mathbf{i}}|$ (typically <0.05), which disappear by increasing the lattice size. A direct transition between the paramagnetic and the antiferromagnetic phases is therefore observed [33] for linear dimensions larger than $L = 8$. In contrast, in our calculations away from half-filling, $|m_{\mathbf{i}}|$ can reach values close to unity. By performing calculations for lattice sizes up to $L^3 = 14^3$, we did not find any dependence of the general properties of the disordered magnetic phase on the lattice size.

The converged disordered magnetic state of lowest energy always shows a gradual increase of $|S_z(\mathbf{k})|$ at $\mathbf{k} = (\pi/a, \pi/a, \pi/a)$ for $\Delta/t \gtrsim 2$ and $U/t \gtrsim 7$. This indicates that weak antiferromagnetic correlations start to build up among the magnetic moments of some sites. To understand in depth the origin of the disordered magnetic phase and its peculiar dependence on Δ/t and U/t, we analyze some quantities directly related to the microscopic properties of the system. More specifically, we consider the mean charge and the mean magnetic moment per site of on-site energy ϵ:

$$n(\epsilon) = \frac{1}{N_\epsilon} \sum_{\epsilon_{\mathbf{i}}=\epsilon} \langle \hat{n}_{\mathbf{i}} \rangle \;, \qquad m(\epsilon) = \frac{1}{N_\epsilon} \sum_{\epsilon_{\mathbf{i}}=\epsilon} \langle m_{\mathbf{i}} \rangle. \qquad (36)$$

N_ϵ is there the number of sites with on-site energy equal to ϵ. We also compute the following quantity

$$A_F(\epsilon) = \frac{1}{2} \frac{1}{N_F} \frac{1}{N_\epsilon} \sum_{\sigma=\uparrow\downarrow} \sum_{\alpha=F} \sum_{\epsilon_{\mathbf{i}}=\epsilon} |u_{\alpha\mathbf{i}\sigma}|^2 \;, \qquad (37)$$

where N_F is the number of eigenstates, whose eigenvalues are equal to the Fermi energy, and the sum over α is restricted to these states. $A_F(\epsilon)$ tells us the on-site energy of the states that contribute to the conductivity in the metallic phase. As

explained better in the following, the comparison of $m(\epsilon)$ and $A_F(\epsilon)$ allows us to understand the interplay between magnetism and metallicity. Additional information on the microscopic properties and on the behavior of the system can also be obtained through the histograms displaying the average number of sites that present any occupation between 0 and 2. These tell us how the charge is shared among the different sites, i.e., how many sites of the lattice are on average (almost) empty, half filled, and fully filled. We distinguish three different cases: large disorder, moderate disorder, and low disorder.

1. Large disorder

In the first place, we examine the limiting case of very large disorder. Figure 4 shows the curve $n(\epsilon)$ and $m(\epsilon)$ at $\Delta/t = 8$ and for $U/t = 4$, $U/t = 8$, and $U/t = 12$. The results are averaged over 40 different disorder realizations. For such large Δ/t, the system is an Anderson insulator (see Fig. 2). For $U/t = 4$, $n(\epsilon)$ increases monotonically from 0 to 2 when ϵ decreases. Sites with very high on-site energies are empty, while sites with very low on-site energy are doubly occupied. Intermediate values of ϵ correspond to partially filled sites. In Fig. 2, $m(\epsilon)$ shows a peak when $n(\epsilon) \sim 1$, indicating that the half-filled sites, i.e., the sites with one electron, are the mostly spin polarized and they play a fundamental role in determining the magnetic properties of the model. The histogram of the site occupations shows that half of the sites of the lattice are completely (or almost completely) empty, while the others are partially filled. There are few sites almost half filled, which sustain a magnetic moment. The appearance of these half-filled states drives the paramagnetic-magnetic transition.

The physics becomes much more interesting when we make U/t larger. As shown in Fig. 4, for $U/t = 8$ and $U/t = 12$, the curve $n(\epsilon)$ is characterized by three plateaus for which we have $n \sim 0$, $n \sim 1$ and $n \sim 2$. At the same time, the histogram presents three peaks indicating that the majority of
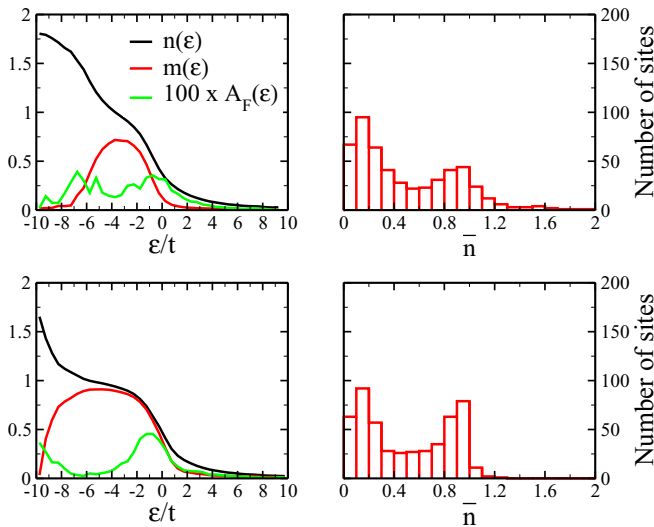
FIG. 5. Left-hand side: Mean charge $n(\epsilon)$, magnetization $m(\epsilon)$, and $A_F(\epsilon)$ (multiplied by 100). Right-hand side: Histograms displaying the average number of sites that have a given occupation $\bar{n}$ between 0 and 2 (the bin width is 0.1). The results are for $\Delta/t = 3$ and $U/t = 6$ (upper panels), $\Delta/t = 3$ and $U/t = 10$ (lower panels).
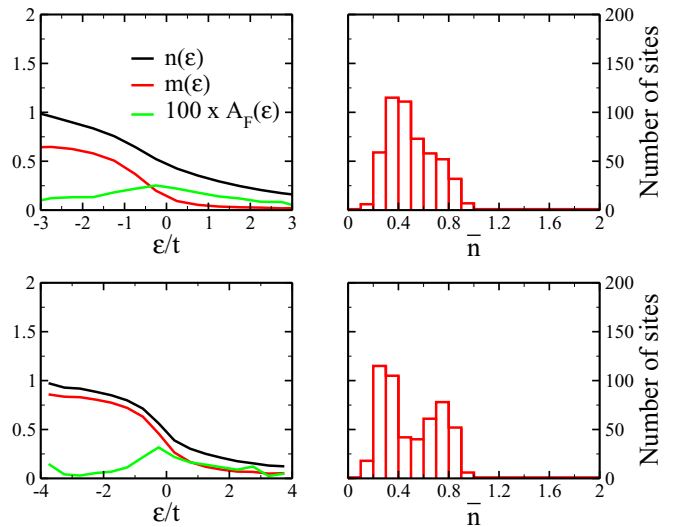

FIG. 6. Left-hand side: Mean charge $n(\epsilon)$, magnetization $m(\epsilon)$, and $A_F(\epsilon)$ (multiplied by 100). Right-hand side: Histograms displaying the average number of sites that have a given occupation $\bar{n}$ between 0 and 2 (the bin width is 0.1). The results are for: $\Delta/t = 1$ and $U/t = 6$ (upper panels), $\Delta/t = 1$ and $U/t = 10$ (lower panels).

the sites are either empty, singly, or doubly occupied. This is the result of the Hubbard-like interaction, which favors integer site occupation. Since empty and doubly occupied sites do not carry any magnetic moment, the only sites contributing to the magnetic properties are the half-filled ones, which assume an antiferromagnetic Neel-type order. In this case, $|S_z(\mathbf{k})|$ indeed features a peak at $\mathbf{k} = (\pi/a, \pi/a, \pi/a)$ similar to that in the example of Fig. 1(b).

2. Moderate disorder

Next we make Δ/t smaller and the system becomes metallic (see Fig. 2). Figure 5 displays $n(\epsilon)$ and $m(\epsilon)$ for $U/t = 6$ and $U/t = 10$ with $\Delta/t = 3$. We now note that sites almost never have on-site energies so low or so high to be either doubly occupied or empty. The curve $n(\epsilon)$ also becomes less steep between plateaus. This is also reflected in the histograms of the site occupations. There are no sites with double occupancy and the number of almost empty sites is strongly reduced as compared to the histograms of Fig. 4. Furthermore, although the majority of the sites have occupancy equal to either $0.1 - 0.2$ or 1, we have many sites with occupancy between 0.3 and 0.6.

Figure 5 also shows $A_F(\epsilon)$ (multiplied by 100 for better display). This presents local maxima in regions where $n(\epsilon)$ varies rapidly and a minimum in correspondence of the plateau for $n \sim 1$. This behavior is very interesting because it indicates that singly occupied sites, which carry large magnetic moments, do not contribute strongly to the state at the Fermi level and hence to the conductivity of the system. Charge transport can occur only through sites with mean charge density $n(\epsilon) \sim 0.2 - 0.6$. In other words, the system has two components: the first is insulating and almost completely spin polarized, while the second is metallic (or at least electrons are more delocalized). This result, which is also found at half-filling [32], is clearly reminiscent of the two-fluids model [35].

Again, with increasing U/t, the appearance of a large number of singly occupied sites produces an enhanced peak of $|S_z(\mathbf{k})|$ at $\mathbf{k} = (\pi/a, \pi/a, \pi/a)$. This originates from the development of antiferromagnetic order between those sites, which belong to the insulating component of the two fluids. For large disorder, as we discussed previously when explaining Fig. 4, the metallic component is strongly suppressed since very few sites have an intermediate charge density n between 0.2 and 0.6 and the physics is completely dominated by the insulating component of the two fluids.

3. Low disorder

Finally, in Fig. 6 we display the results for $\Delta/t = 1$ and for $U/t = 6$. In this range, $n(\epsilon)$ changes monotonically and smoothly between about 0.2 and 0.8. As shown by the histogram, we find that most of the sites have an occupation equal to ~ 0.4. Furthermore, the function $A_F(\epsilon)$, plotted in Fig. 6, is a slowly varying function. This indicates that all the sites have nonzero weight in the state at the Fermi level and that the metallic component of the two fluids dominates the physics. Indeed, no enhanced peak for $|S_z(\mathbf{k})|$ at $\mathbf{k} = (\pi/a, \pi/a, \pi/a)$ can be found. A sign of the tendency of the system to the formation of the two fluids can be seen only by increasing the interaction up to $U/t = 10$ (see Fig. 6). The histogram of site occupations indicates that the system starts to decompose into two subsystems with different site occupancy ($n \sim 0.2$ and $n \sim 0.7$). At the same time, $A_F(\epsilon)$ shows an increasing weight coming from sites with $n \sim 0.5$.

IV. MAGNETIC EXCITATIONS

In this section, we investigate the magnetic excitations. We distinguish two types of magnetic excitations: spin waves (of collective character) and Stoner excitations (single particle
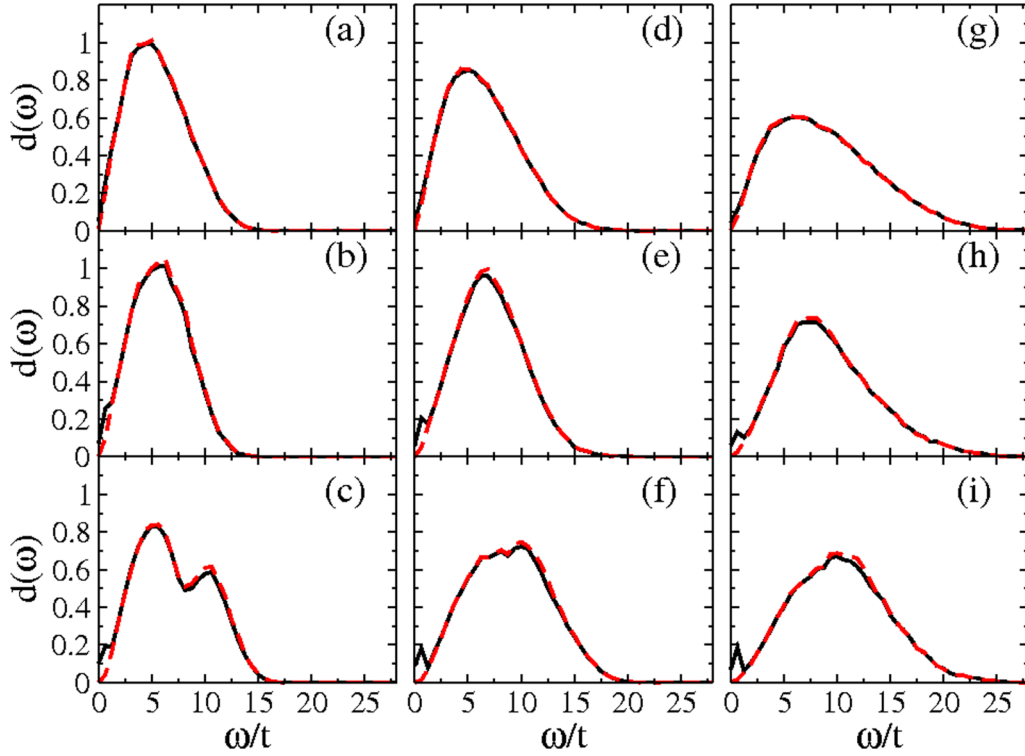
FIG. 7. DOS of the BSE (black line) and the MF excitations (red dashed line) for $\Delta/t = 2$, $U/t = 4$ (a), $\Delta/t = 2$, $U/t = 8$ (b), $\Delta/t = 2$, $U/t = 12$ (c), $\Delta/t = 4$, $U/t = 4$ (d), $\Delta/t = 4$, $U/t = 8$ (e), $\Delta/t = 4$, $U/t = 12$ (f), $\Delta/t = 6$, $U/t = 4$ (g), $\Delta/t = 6$, $U/t = 8$ (h), $\Delta/t = 6$, $U/t = 12$ (i). The DOS is averaged over 50 disorder configurations.

excitations). The main question is whether spin waves can emerge in an impurity band.

The energy of a Stoner excitation is readily obtained from the difference between the energy of an unoccupied MF state and the energy of an occupied one of opposite spin, $\omega_n^{MF} = E_{p\sigma} - E_{h-\sigma}$. In contrast, the collective magnetic excitations are calculated by solving the BSE. We employ both implementations of the BSE described in Sec. II C. Here, at variance with the previous section, we consider lattices of linear dimension $L = 4$ and $L = 6$. The diagonalization of the RPA matrix introduced in Eq. (25) is an $O(N^3)$ operation and the calculation of the excitation energies is very fast for $L = 4$. However, we cannot perform calculations for lager lattice sizes because of the high computer-memory requirements. The results for $L = 6$ are therefore obtained by using Eq. (16). Unfortunately, the construction of the MF transverse spin susceptibility is an operation that scales as $O(N^4)$ and, therefore, calculations for larger lattices are found to be unfeasible with our implementation and the available computational resources. At the qualitative level, we do not find any difference in the results obtained for $L = 4$ or 6.

We calculate the excitations density of state (DOS) as

$$d(\omega) = \frac{1}{L^3} \sum_n \delta(\omega - \omega_n), \qquad (38)$$

with ω_n being the energy of either a Stoner excitation, $\omega_n = \omega_n^{MF}$, or of a collective magnetic excitation calculated through the BSE. The results are shown in Fig. 7 for various values of

U/t and Δ/t after having averaged over 50 disorder realizations.

Both types of excitations extend down to $\omega = 0$. In the case of the Stoner excitations, this is a consequence of the metallic or Anderson insulating nature of the MF ground state, which implies that there is no energy gap separating the MF highest occupied and lowest unoccupied electronic states. In contrast, in the case of the collective excitations, the zero energy modes are Goldstone modes.

For $U/t = 4$, the MF DOS and the BSE DOS are almost indistinguishable [see Figs. 7(a), 7(d) and 7(g)]. Hence, the magnetic excitations are only of Stoner type and there are no spin waves. This can be further observed in Fig. 8, where only the low energy part of the DOS, calculated for $L = 6$, is displayed. In contrast, for larger U/t, the spectrum obtained from the BSE shows a clear feature at $0 \lesssim \omega \lesssim 1$, which is absent in the MF results. This indicates that spin waves dominate the low-energy region of the magnetic-excitations spectrum before being absorbed into the Stoner band.

A careful examination of the components of the eigenvectors of the RPA matrix, $\{X_{p\uparrow h\downarrow}^n, Y_{p\downarrow h\uparrow}^n\}$, can also be used to determine whether the BSE excitations differ drastically from the MF ones. Equations (26) show that if a mode of energy ω_n is a pure Stoner excitation, only one of the components $|X_{p\uparrow h\downarrow}^n|$ ($|Y_{p\downarrow h\uparrow}^n|$) will be equal to 1 and all the others will vanish. In contrast, for a spin wave, we expect many components different from zero and with an amplitude much smaller than unity. In Fig. 9, we plot the absolute value of the largest component of each eigenvector of the RPA matrix, $|V_{MAX}(\omega_n)| = \max\{|X_{p\uparrow h\downarrow}^n|, |Y_{p\downarrow h\uparrow}^n|\}$, as a function of
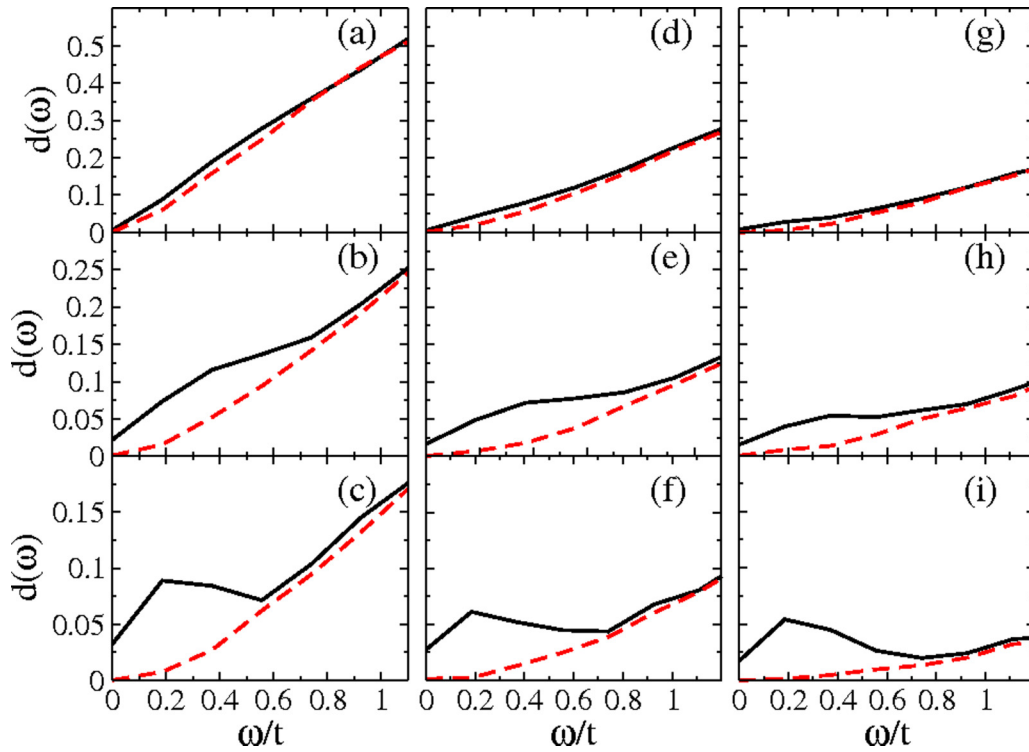
FIG. 8. DOS of the BSE (black line) and the MF excitations (red dashed line) for lattices with $L = 6$ and $\Delta/t = 2$, $U/t = 4$ (a), $\Delta/t = 2$, $U/t = 8$ (b), $\Delta/t = 2$, $U/t = 12$ (c), $\Delta/t = 4$, $U/t = 4$ (d), $\Delta/t = 4$, $U/t = 8$ (e), $\Delta/t = 4$, $U/t = 12$ (f), $\Delta/t = 6$, $U/t = 4$ (g), $\Delta/t = 6$, $U/t = 8$ (h), $\Delta/t = 6$, $U/t = 12$ (i). The DOS is averaged over 50 disorder configurations.

the energy ω/t. Figure 9(a), which refers to $\Delta/t = 2$ and $U/t = 4, 8, 12$, shows very clearly the difference between the excitations for small and large interaction strengths. On the one hand, $|V_{\text{MAX}}(\omega)|$ is a smooth function for $U/t = 4$ and has an almost constant value of about 0.6. On the other hand, it jumps from about 0.2 to about 0.6 at $\omega \sim 1$ for $U/t = 8$ and $U/t = 12$. This indicates a change in the character of the spin excitations and reflects the low-energy feature that is observed in the BSE spectrum and that is absent in the MF one
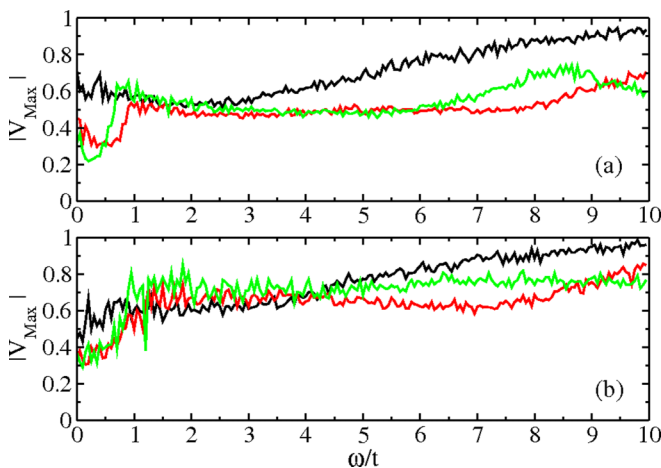

FIG. 9. $|V_{\text{MAX}}(\omega_n)|$ for $\Delta/t = 2$ (a) and $\Delta/t = 6$ (b). The black line corresponds to $U/t = 4$, the red one to $U/t = 8$, and the green one to $U/t = 12$. The results are averaged over 50 disorder configurations.

(compare with the discussion about Figs. 7 and 8). The same holds true also for $\Delta/t = 6$, in spite of the slight decrease of $|V_{\text{MAX}}(\omega)|$ for $U/t = 4$ at low ω and the less steep profile for $U/t = 8, 12$ [see Fig. 9(b)].

Further insights into the nature of the BSE excitations can be obtained by looking at their spatial distribution. By using the unitary transformations Eqs. (5) and (6) we can rewrite the operators $\hat{Q}_n^\dagger$ defined in Eqs. (26), as

$$\hat{Q}_n^\dagger = \sum_{\mathbf{ij}} U_{\mathbf{ij}}^n \hat{c}_{\mathbf{i}\downarrow}^\dagger \hat{c}_{\mathbf{j}\uparrow}, \tag{39}$$

where the coefficients

$$U_{\mathbf{ij}}^n = \sum_{p\uparrow,h\downarrow} X_{p\uparrow h\downarrow}^n u_{p\mathbf{j}\uparrow}^* u_{h\mathbf{i}\downarrow} - \sum_{p\downarrow,h\uparrow} Y_{p\downarrow h\uparrow}^n u_{h\mathbf{j}\downarrow}^* u_{p\mathbf{i}\uparrow} \tag{40}$$

are normalized so that $\sum_{\mathbf{ij}} |U_{\mathbf{ij}}^n|^2 = 1$. As $U_{\mathbf{ij}}^{n*} = \langle n_{\text{RPA}} | \hat{c}_{\mathbf{i}\downarrow}^\dagger \hat{c}_{\mathbf{j}\uparrow} | 0_{\text{RPA}} \rangle$ (for $\omega_n > 0$), we distinguish two "kinds" of collective excitations: (1) the pure spin-wave excitations, whose spatial probability amplitude is given by $U_{\mathbf{ii}}^{n*} = \langle n_{\text{RPA}} | \hat{S}_{\mathbf{i}}^- | 0_{\text{RPA}} \rangle$, while $U_{\mathbf{ij}}^{n*} \approx 0$ for $\mathbf{i} \neq \mathbf{j}$; 2) the excitations that present some degrees of charge transfer and whose spatial probability amplitude is given by $U_{\mathbf{ij}}^{n*} \neq 0$ with $\mathbf{i} \neq \mathbf{j}$. To reveal the nature of the excitations we therefore calculate $S_n = \sum_{\mathbf{i}} |U_{\mathbf{ii}}^n|^2$. When $S_n \ll 1$ the nth excitation involves charge transfer, while for $S_n \approx 1$ it is a pure spin wave. The value of S_n for excitations of energies $0 < \omega_n < 1$ is reported in Table I for some representative points in the $(\Delta/t, U/t)$ phase diagram. For comparison, we have also calculated the weights of the Stoner excitations in the on-site

TABLE I. S_n of the BSE excitations of energies $0 < \omega_n < 1$ for selected points in the $(\Delta/t, U/t)$ phase diagram. The results are averaged over 50 disorder configurations.

	$U/t = 4$	$U/t = 8$	$U/t = 12$
$\Delta/t = 2$	0.05	0.32	0.3
$\Delta/t = 4$	0.1	0.43	0.67
$\Delta/t = 6$	0.21	0.48	0.69

spin-flip subspace. This is given by

$$S_n^{\mathrm{MF}} = \sum_{\mathbf{i}} |\langle n_{\mathrm{MF}}|\hat{c}_{\mathbf{i}\downarrow}^{\dagger}\hat{c}_{\mathbf{i}\uparrow}|0_{\mathrm{MF}}\rangle|^2 = \sum_{\mathbf{i}} |u_{h\mathbf{i}\uparrow}|^2|u_{p\mathbf{i}\downarrow}|^2 \quad (41)$$

for an excitation of energy $\omega_n^{\mathrm{MF}} = E_{p\downarrow} - E_{h\uparrow}$. The results are listed in Table II.

We can observe that S_n is of the same order of magnitude of S_n^{MF} for $U/t = 4$ and $\Delta/t = 4$. This indicates that the spin excitations are not just characterized by a large off-site contribution, but are mainly of Stoner type. In contrast, upon increasing either Δ/t or U/t, S_n becomes at least one order of magnitude larger than S_n^{MF}. Low-energy excitations then tend to become true spin-wave excitations. On the one hand, the reduction of the charge-transfer character of the excitations for large disorder reflects the increase of the localization of the MF states. On the other hand, when U/t is large, excitations involving charge-transfer are projected out of the spectrum. This analysis complements the calculation of the DOS and gives a more quantitative and microscopic view on the magnetic excitations.

V. CONCLUSIONS AND PERSPECTIVES

Our results show that an impurity band described by the AHM undergoes a magnetic transition at specific values of U/t and of Δ/t. This transition is not an artifact of the small size of the lattices considered, but it is robust against finite-size scaling and it survives in the thermodynamic limit. Two different behaviors can be identified in the magnetic phase:

(1) For small values of the interaction strength (i.e., $U/t \lesssim 4$) the system is metallic or Anderson insulating. Most of the sites are filled with less than one electron. Only very few sites host one full electron and develop a magnetic moment. However, these magnetic moments are very diluted and no long-range magnetic order (ferromagnetic or antiferromagnetic) is found. The system has then a rather "disordered" magnetic structure. A detailed analysis of this magnetic phase goes beyond the scope of the present work.

TABLE II. S_n^{MF} of the MF excitations of energies $0 < \omega_n^{\mathrm{MF}} < 1$ for selected points in the $(\Delta/t, U/t)$ phase diagram. The results are averaged over 50 disorder configurations.

	$U/t = 4$	$U/t = 8$	$U/t = 12$
$\Delta/t = 2$	0.02	0.01	0.01
$\Delta/t = 4$	0.02	0.008	0.005
$\Delta/t = 6$	0.02	0.009	0.004

(2) For large values of the interaction strength, namely for $U/t > 4$, there are many sites, where the electrons are strongly localized. Large magnetic moments develop at such sites. An antiferromagnetic order is established between some of those sites and a clear spin-wave feature emerges in the low-energy region of the spectrum of the magnetic excitations. At the same time, there are also a cluster of sites where electrons can be more delocalized and no magnetic moments appear. This "phase-separation" between the lattice sites clearly reminds us of the two-fluid model proposed originally for doped Si.

We suggest that the second scenario may be relevant for impurity bands in OSCs, where U/t is generally large because of the weak electronic screening and the small overlap of the impurity wave functions.

Within the two-fluid picture, we expect that if a region with delocalized electrons percolates through the entire system, a path for charge transport will be established. Conversely, when the concentration of localized magnetic moments becomes large, spin waves will enable transport of pure spin currents. A quantitative estimate of the impurities required to observe charge and spin transport in real devices is unfortunately not possible from the calculations we have presented here as it would require multiscale simulations with material-specific parameters obtained from first principles [60–62]. This task goes beyond the goal of the paper and we leave it for future studies.

Besides addressing the transport characteristics, we believe that important progress in understanding the role of the impurity bands in OSCs may come from the study of the magnetic properties. For example, the extension of our work to finite temperature may provide predictions for the static and dynamic susceptibility, two quantities that can be directly validated by experiments.

The two-fluid picture shares some similarities with the model proposed by Yu [27,28]. In both cases, the charge diffusion is due to hopping, while the spin diffusion is mediated by the magnetic coupling between localized magnetic moments. Nonetheless, there are some notable differences. In the model of Yu, disorder is not explicitly taken into account and each impurity is assumed to present a localized magnetic moment coupled via direct exchange to that of the neighboring impurities. In contrast, the magnetic moments in the two-fluid picture form only at some impurities as a results of the interplay between disorder and electron-electron interaction and the magnetic interaction is mostly driven by super-exchange rather then by direct exchange.

In conclusion, both theory and experiments are now converging toward the understanding that spin transport in hybrid organic spin valves comprising Alq_3, and maybe also in other OSCs, proceeds via an impurity band. The challenge ahead for theory consists of extending the current models to include material-specific properties obtained from first-principles calculations to perform quantitative comparisons with the experimental results.

---

[1] V. Dediu, M. Murgia, F. C. Matacotta, C. Taliani, and S. Barbanera, Solid State Commun. **122**, 181 (2002).

[2] V. Dediu, L. E. Hueso, I. Bergenti, and C. Taliani, Nat. Mater. **8**, 707 (2009).

[3] S. Sanvito, Chem. Soc. Rev. **40**, 3336 (2011).

[4] Z. H. Xiong, D. Wu, Z. Valy Vardeny, and J. Shi, Nature **427**, 821 (2004).

[5] V. Dediu, L. E. Hueso, I. Bergenti, A. Riminucci, F. Borgatti, P. Graziosi, C. Newby, F. Casoli, M. P. De Jong, C. Taliani, and Y. Zhan, Phys. Rev. B **78**, 115203 (2008).

[6] D. Sun, L. Yin, C. Sun, H. Guo, Z. Gai, X.-G. Zhang, T. Z. Ward, Z. Cheng, and J. Shen, Phys. Rev. Lett. **104**, 236602 (2010).

[7] R. Lin, F. Wang, J. Rybicki, M. Wohlgenannt, and K. A. Hutchinson, Phys. Rev. B **81**, 195214 (2010).

[8] M. Gobbi, F. Golmar, R. Llopis, F. Casanova, and L. E. Hueso, Adv. Mater. **23**, 1609 (2011)

[9] X. Sun, M. Gobbi, A. Bedoya-Pinto, O. Txoperena, F. Golmar, R. Llopis, A. Chuvilin, F. Casanova, and L. E. Hueso, Nat. Commun. **4**, 2794 (2013).

[10] T. D. Nguyen, E. Ehrenfreund, and Z. V. Vardeny, Science **337**, 204 (2012).

[11] M. Cinchetti, K. Heimer, J.-P. Wüstenberg, O. Andreyev, M. Bauer, S. Lach, C. Ziegler, Y. Gao, and M. Aeschlimann, Nat. Mater. **8**, 115 (2009).

[12] A. J. Drew, J. Hoppler, L. Schulz, F. L. Pratt, P. Desai, P. Shakya, T. Kreouzis, W. P. Gillin, A. Suter, N. A. Morley, V. K. Malik, A. Dubroka, K. W. Kim, H. Bouyanfif, F. Bourqui, C. Bernhard, R. Scheuermann, G. J. Nieuwenhuys, T. Prokscha, and E. Morenzoni, Nat. Mater. **8**, 109 (2009).

[13] Y. Q. Zhan, X. J. Liu, E. Carlegrim, F. H. Li, I. Bergenti, P. Graziosi, V. Dediu, and M. Fahlman, Appl. Phys. Lett. **94**, 053301 (2009).

[14] Y. Q. Zhan, I. Bergenti, L. E. Hueso, V. Dediu, M. P. de Jong, and Z. S. Li, Phys. Rev. B **76**, 045406 (2007).

[15] C. Barraud, P. Seneor, R. Mattana, S. Fusil, K. Bouzehouane, C. Deranlot, P. Graziosi, L. Hueso, I. Bergenti, V. Dediu, F. Petroff, and A. Fert, Nat. Phys. **6**, 615 (2010).

[16] S. Sanvito, Nat. Phys. **6**, 562 (2010).

[17] P. P. Ruden, J. Appl. Phys. **95**, 4898 (2004).

[18] S. Steil, N. Großmann, M. Laux, A. Ruffing, D. Steil, M. Wiesenmayer, S. Mathias, O. L. A. Monti, M. Cinchetti, and M. Aeschlimann, Nat. Phys. **9**, 242 (2013).

[19] S. Müller, S. Steil, A. Droghetti, N. Großmann, S. Sanvito, V. Meded, A. Magri, B. Schäfer, O. Fuhr, M. Ruben, M. Cinchetti, and M. Aeschlimann, New. J. Phys. **15**, 113054 (2013).

[20] A. Droghetti, S. Steil, N. Großmann, N. Haag, H. Zhang, M. Willis, W. P. Gillin, A. J. Drew, M. Aeschlimann, S. Sanvito, and M. Cinchetti, Phys. Rev. B **89**, 094412 (2014).

[21] A. Droghetti, P. Thielen, I. Rungger, N. Haag, N. Großmann, J. Stöckl, B. Stadtmüller, M. Aeschlimann, S. Sanvito, and M. Cinchetti, Nat. Commun. **7**, 12668 (2016).

[22] A. Droghetti, I. Rungger, M. Cinchetti, and S. Sanvito, Phys. Rev. B **91**, 224427 (2015).

[23] L. E. Hueso, I. Bergenti, A. Riminucci, Y. Q. Zhan, and V. Dediu, Adv. Mater. **19**, 2639 (2007).

[24] M. Prezioso, A. Riminucci, I. Bergenti, P. Graziosi, D. Brunel, and V. A. Dediu, Adv. Mater. **23**, 1371 (2011).

[25] A. Droghetti, M. Cinchetti, and S. Sanvito, Phys. Rev. B **89**, 245137 (2014).

[26] G. Schmidt, D. Ferrand, L. W. Molenkamp, A. T. Filip, and B. J. van Wees, Phys. Rev. B **62**, R4790(R) (2000).

[27] Z. G. Yu, Nature Commun. **5**, 4842 (2014).

[28] Z. G. Yu, Phys. Rev. Lett. **111**, 16601 (2013).

[29] A. Riminucci, P. Graziosi, M. Calbucci, R. Cecchini, M. Prezioso, F. Borgatti, I. Bergenti, and V. A. Dediu, Appl. Phys. Lett. **112**, 209901 (2018).

[30] I. Bergenti, F. Borgatti, M. Calbucci, A. Riminucci, R. Cecchini, P. Graziosi, D. A. MacLaren, A. Giglia, J. P. Rueff, D. Ceolin, L. Pasquali, and V. A. Dediu, ACS Appl. Mater. Interfaces **10**, 8132 (2018).

[31] A. Riminucci, Z.-G. Yu, M. Prezioso, R. Cecchini, I. Bergenti, P. Graziosi, and V. A. Dediu, ACS Appl. Mater. Interfaces **11**, 8319 (2019).

[32] M.A. Tusch and D. E. Logan, Phys. Rev. B **48**, 14843 (1993).

[33] D. G. Rowan, Y. H. Szczech, M. A. Tusch, and D. E. Logan, J. Phys.: Condens. Matter **7**, 6853 (1995)

[34] M. Milovanovíc, S. Sachdev, and R. N. Bhatt, Phys. Rev. Lett. **63**, 82 (1989).

[35] M. A. Paalanen, R. N. Bhatt, and S. Sachdev, Physica B **169**, 223 (1991).

[36] M. A. Paalanen, S. Sachdev, R. N. Bhatt, and A. E. Ruckenstein, Phys. Rev. Lett. **57**, 2061 (1986).

[37] M. J. Hirsch, D. F. Holcomb, R. N. Bhatt, and M. A. Paalanen, Phys. Rev. Lett. **68**, 1418 (1992).

[38] M. A. Paalanen, J. E. Graebner, R. N. Bhatt, and S. Sachdev, Phys. Rev. Lett. **61**, 597 (1988).

[39] R. N. Bhatt and P. A. Lee, Phys. Rev. Lett. **48**, 344 (1982).

[40] D. Sun, E. Ehrenfreund, and Z. V. Vardeny, Chem. Commin **50**, 1781 (2014).

[41] S. Watanabe, K. Ando, K. Kang, S. Mooser, Y. Vaynzof, H. Kurebayashi, E. Saitoh, and H. Sirringhaus, Nat. Phys. **10**, 308 (2014).

[42] D. Sun, K. J. van Schooten, M. Kavand, H. Malissa, C. Zhang, M. Groesbeck, C. Boehme, and Z. V. Vardeny, Nat. Mater. **15**, 863 (2016).

[43] D. Sun, C. M. Kareis, K. J. van Schooten, W. Jiang, G. Siegel, M. Kavand, R. A. Davidson, W. W. Shum, C. Zhang, H. Liu, A. Tiwari, C. Boehme, F. Liu, P. W. Stephens, J. S. Miller, and Z. V. Vardeny, Phys. Rev. B **95**, 054423 (2017).

[44] T. Moriya, *Spin Fluctuations in Itinerant Electron Magnetism* (Springer-Verlag, Berlin, 1985).

[45] J. W. Negele and H. Orland, *Quantum Many-Particle System* (Advanced Book Program, Westview Press, Boulder, CO, 1998).

[46] C. Gaul, S. Hutsch, M. Schwarze, K. S. Schellhammer, F. Bussolotti, S. Kera, G. Cuniberti, K. Leo, and F. Ortmann, Nat. Mater. **17**, 439 (2018).

[47] H. Oberhofer, K. Reuter, and J. Blumberger, Chem. Rev. **117**, 10319 (2017).

[48] F. Ortmann, F. Bechstedt, and K. Hannewald, Phys Status Solidi **248**, 511 (2011).

[49] R. M. White, *Quantum Theory of Magnetism: Magnetic Properties of Materials* (Springer-Verlag, Berlin, 2007).

[50] S. Doniach and E. H. Sondheimer, *Green's Functions for Solid State Physicists* (Imperial College Press, London, 1998).

[51] Y. H. Szczech, M. A. Tusch, and D. E. Logan, J. Phys.: Condens. Matter **9**, 9621 (1997).

[52] D. J. Rowe, *Nuclear Collective Motion: Models and Theory* (Methuen, London, 1970)

[53] P. Ring and P. Schuck, *The Nuclear Many-Body Problem*, 3rd ed. (Springer-Verlag, Berlin, 2004).

[54] A. Droghetti, Ph.D. thesis, Trinity College, Dublin, 2012.

[55] K. Byczuk, W. Hofstetter and D. Vollhardt, *Anderson Localization vs. Mott-Hubbard Metal-Insulator Transition in Disordered, Interacting Lattice Fermion Systems in 50 Years of Anderson Localization*, edited by E. Abrahams (World Scientific, Singapore, 2010), Chap. 20; also available in Int. J. Mod. Phys. B **24**, 1727 (2010).

[56] D. R. Penn, Phys. Rev. **142**, 350 (1966).

[57] C. Dasgupta and J. W. Halley, Phys. Rev. B **47**, 1126 (1993).

[58] M. Berciu and R. N. Bhatt, Phys. Rev. B **69**, 045202 (2004).

[59] T. M. Chang, J. D. Bauer, and J. L. Skinner, J. Chem. Phys. **93**, 8973 (1990).

[60] C. Motta and S. Sanvito, J. Chem. Theo. Comp. **10**, 4624 (2014).

[61] S. Roychoudhury and S. Sanvito, Phys. Rev. B **95**, 085126 (2017).

[62] S. Roychoudhury and S. Sanvito, Phys. Rev. B **98**, 125204 (2018).